

Profile measurements in the plasma edge of mega amp spherical tokamak using a ball pen probe

N. R. Walkden, J. Adamek, S. Allan, B. D. Dudson, S. Elmore, G. Fishpool, J. Harrison, A. Kirk, and M. Komm

Citation: [Review of Scientific Instruments](#) **86**, 023510 (2015);

View online: <https://doi.org/10.1063/1.4908572>

View Table of Contents: <http://aip.scitation.org/toc/rsi/86/2>

Published by the [American Institute of Physics](#)

Articles you may be interested in

[Profile measurements of the electron temperature on the ASDEX Upgrade, COMPASS, and ISTTOK tokamak using Thomson scattering, triple, and ball-pen probes](#)

[Review of Scientific Instruments](#) **87**, 043510 (2016); 10.1063/1.4945797

[Design and validation of the ball-pen probe for measurements in a low-temperature magnetized plasma](#)

[Review of Scientific Instruments](#) **84**, 013505 (2013); 10.1063/1.4775491

[Divertor plasma detachment](#)

[Physics of Plasmas](#) **23**, 055602 (2016); 10.1063/1.4948273

[Comparative measurements of plasma potential with ball-pen and Langmuir probe in low-temperature magnetized plasma](#)

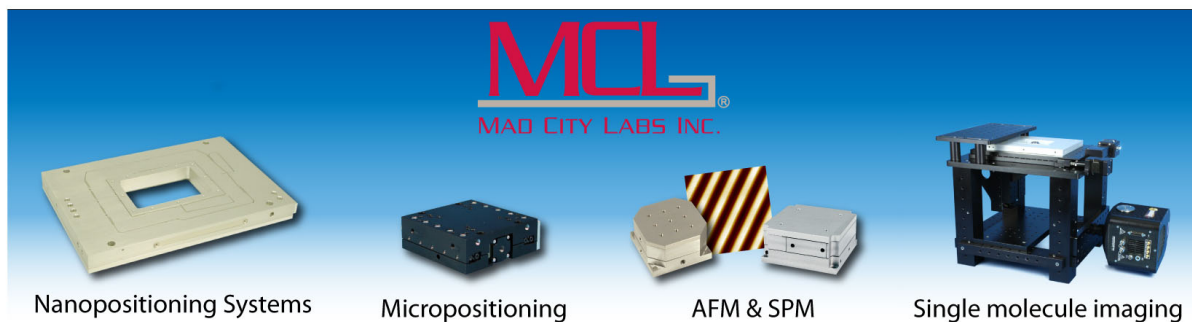
[Physics of Plasmas](#) **22**, 033516 (2015); 10.1063/1.4916572

[Design and fabrication of a new compound probe for plasma flux measurement in IR-T1 tokamak](#)

[Review of Scientific Instruments](#) **88**, 093516 (2017); 10.1063/1.4994037

[Scanning ion sensitive probe for plasma profile measurements in the boundary of the Alcator C-Mod tokamak](#)

[Review of Scientific Instruments](#) **84**, 053507 (2013); 10.1063/1.4807699



Profile measurements in the plasma edge of mega amp spherical tokamak using a ball pen probe

N. R. Walkden,^{1,2,a)} J. Adamek,³ S. Allan,¹ B. D. Dudson,² S. Elmore,¹ G. Fishpool,¹ J. Harrison,¹ A. Kirk,¹ and M. Komm³

¹*CCFE, Culham Science Centre, Abingdon, Oxon OX14 3DB, United Kingdom*

²*Department of Physics, York Plasma Institute, University of York, Heslington, York YO10 5DD, United Kingdom*

³*Institute of Plasma Physics of AS CR, v. v. i., Za Slovankou 3, 182 00 Praha 8, Czech Republic*

(Received 8 December 2014; accepted 5 February 2015; published online 25 February 2015)

The ball pen probe (BPP) technique is used successfully to make profile measurements of plasma potential, electron temperature, and radial electric field on the Mega Amp Spherical Tokamak. The potential profile measured by the BPP is shown to significantly differ from the floating potential both in polarity and profile shape. By combining the BPP potential and the floating potential, the electron temperature can be measured, which is compared with the Thomson scattering (TS) diagnostic. Excellent agreement between the two diagnostics is obtained when secondary electron emission is accounted for in the floating potential. From the BPP profile, an estimate of the radial electric field is extracted which is shown to be of the order ~ 1 kV/m and increases with plasma current. Corrections to the BPP measurement, constrained by the TS comparison, introduce uncertainty into the E_R measurements. The uncertainty is most significant in the electric field well inside the separatrix. The electric field is used to estimate toroidal and poloidal rotation velocities from $\mathbf{E} \times \mathbf{B}$ motion. This paper further demonstrates the ability of the ball pen probe to make valuable and important measurements in the boundary plasma of a tokamak. [<http://dx.doi.org/10.1063/1.4908572>]

I. INTRODUCTION

The plasma potential plays an important role in many of the processes occurring in the tokamak plasma edge. In the electrostatic limit of the two-fluid equations appropriate to the plasma edge,^{1–3} the $\mathbf{E} \times \mathbf{B}$ velocity, with $\mathbf{E} = -\nabla\phi$, where ϕ is the plasma potential, provides the dominant advective flow and determines the dynamics of both turbulence⁴ and individual filaments.⁵ On the equilibrium scale gradients in the radial electric field can lead to a strongly sheared flow close to the separatrix, commonly termed the radial shear layer. Despite its important role in edge physics, the plasma potential has remained a difficult quantity to measure accurately on either the fluctuation or equilibrium scale. The ball pen probe (BPP), developed by Adamek *et al.*^{6,7} offers a diagnostic technique capable of measuring the plasma potential with a robust implementation that may withstand particle and heat fluxes from the plasma at radii up to and within the separatrix. The BPP technique has previously been tested simultaneously with an emissive probe⁷ and a self-emitting Langmuir probe⁸ and shows excellent agreement in each case. The robustness of the BPP design against the high particle and heat fluxes in the plasma edge as well as its relative simplicity in design makes it an attractive option over the emissive probe, which can rarely be operated near to the separatrix due to its inherently weak structure. The BPP technique has been used on the CASTOR,^{6,9} ASDEX-Upgrade,^{10–12} ISTTOK,¹³ and COMPASS^{8,14} tokamaks and in the torsatron TJ-K, alongside two other low temperature plasma devices.¹⁵

In this paper, results are presented from the development and operation of a BPP on the Mega Amp Spherical Tokamak (MAST).¹⁶ MAST, being a tight aspect ratio tokamak, has a reduced magnetic field strength on the low field side compared to both ASDEX-Upgrade and CASTOR but has electron and ion temperatures of the same magnitude. Consequently, the ion (and electron) Larmor radius, ρ_i on MAST is larger than in the previous two devices, but (unlike TJ-K) the ions remain fully magnetized. This makes MAST an ideal intermediate test of the BPP technique.

In Sec. II, the BPP design for MAST is described. In Sec. III, plasma potential profile measurements are presented and compared to the standard floating potential measurement from a Langmuir probe. In Sec. IV, the electron temperature calculated from the BPP signals is presented and a comparison with the Thomson scattering (TS) diagnostic on MAST is used to determine the success of the BPP measurement. Section V presents the radial electric field as measured with the BPP. Section VI discusses the BPP results before Sec. VII concludes.

II. THE BALL PEN PROBE ON MAST

The BPP, shown in Figure 1, is not a bespoke design but rather a modification of the Gundestropp probe previously used on MAST.¹⁷ The BPP pins in the probe built for MAST have flat collection surfaces recessed inside a ceramic body, making it similar in design to the BPP used in CASTOR.⁹ The retraction depths of the BPP pins are fixed below the ion Larmor radius. The essential features defining a BPP are a retracted collector inside a ceramic shielding tube. In the

^{a)}Email: nrw504@york.ac.uk

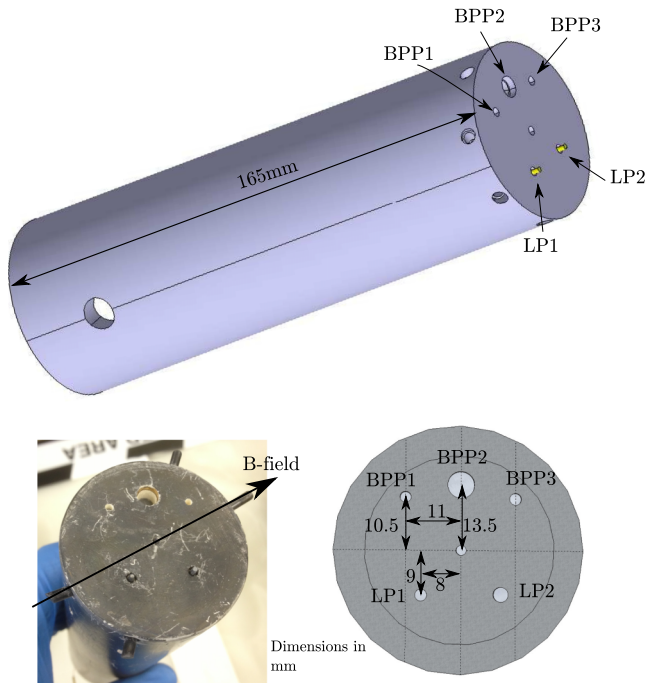


FIG. 1. The BPP design for MAST consists of an array of recessed BPPs and standard Langmuir probes (LPs). BPP pins are ball pen probes, whilst LP1 and LP2 are standard Langmuir probes. Pins BPP1, BPP2, BPP3, and LP1 are floating pins, whilst LP2 may be externally biased. All unlabeled pins were unused during the experiments commented upon within this paper.

BPP described here, the collectors are graphite, whilst the shielding tube is boron nitride. Outer surfaces are coated with a thin layer of carbon to prevent excess impurity accumulation in the plasma. Inner surfaces of the shielding tube are bare boron nitride. The dielectric shielding prevents an independent external biasing of the tube from the collector surface. The retraction depths and collector diameters for the three BPP pins on the MAST probe are given in Table I. Pin LP2 was the only pin attached to an external power supply and could be biased, whilst LP1 as well as the BPP pins was operated in floating mode for the entirety of the experiments presented, herein. Of the three BPP pins, BPP1 and BPP3 were found to exhibit suppression of the signal over the entire frequency spectrum as a result of excessively high pin impedances. This could be rectified in future implementations through use of a high impedance ($T\Omega$) electrometer, as used in Ref. 15, acting as a voltage buffer. This was noted after the experiments detailed so this modification could not be made at the time. The wider diameter of pin BPP2 significantly reduced the effective pin impedance and the suppression of the low frequency component of the signal was not observed.

TABLE I. MAST BPP pin retraction depths and diameters. Since the pin retraction and diameter were fixed in each case, a suitable range of parameters was chosen for the three pins to allow maximum flexibility.

Pin	Depth (mm)	Diameter (mm)
BPP1	2	1.5
BPP2	5	4
BPP3	8	1.5

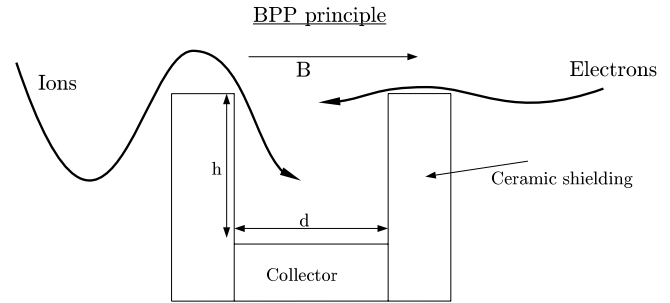


FIG. 2. Cross section of the ball pen probe principle. The collector is retracted inside a ceramic shielding tube by a distance larger than the ion Larmor radius.

Suppression of high frequency part of the BPP spectrum was noted in the colder SOL region of the plasma; however, this did not affect profile measurements.

The floating potential of a probe in a plasma, which arises by the constraint of ambipolarity, is given by Ref. 18,

$$V_{fl} = \phi - \alpha T_e, \quad (1)$$

where V_{fl} is the floating voltage on the probe, ϕ is the plasma potential, T_e is the electron temperature in eV , and $\alpha = \ln(I_e/I_i)$ is the logarithmic ratio of electron to ion currents flowing to the probe. In a magnetized plasma, the dominant flux of electrons and ions to an exposed probe, such as a Langmuir probe, occurs along magnetic field lines. This leads to sheath formation as a result of the high electron mobility compared to the ions. Neglecting for now the effect of secondary electron emission, α_{LP} is given in the case of a Langmuir probe by Ref. 19,

$$\alpha = \ln\left(\frac{I_e}{I_i}\right) = -\frac{1}{2} \ln\left(2\pi \frac{m_e}{m_i} \left(1 + \frac{T_i}{T_e}\right)\right). \quad (2)$$

The goal of the BPP is to reduce α to zero by equalizing the ratio of electron to ion currents at the collector. This is achieved by shielding the collector from fluxes directed along the magnetic field line such that cross-field transport is required for the net collection of ions and electrons. This principle is illustrated in Figure 2. The results of 2D particle-in-cell simulations^{20,21} of a BPP suggest that Eq. (1) holds as the BPP is retracted inside the probe surface, and significant experimental evidence supports the use of Eq. (1) in a BPP. For the purposes of this paper, Eq. (1) will be assumed to apply in the absence of a first principles model for the BPP. Since no current model exists to predict α_{BPP} , this must be treated as a free parameter in this study. In previous studies, α_{BPP} has been measured directly^{6,7,9} by applying an external voltage sweep to the BPP; however, this is not possible in the present implementation. Instead, α_{BPP} will be constrained by a detailed cross-diagnostic comparison with the Thomson scattering system on MAST.²²

The results in this paper are drawn from three connected double-null (CDN) Ohmic L-mode plasmas on MAST. These are shot numbers: 28 819, 28 830, and 28 834. The relevant details of these shots are given in Table II. The three shots represent both a two-point plasma current and a two-point electron density scan Ohmic L-mode. The BPP was attached to the end of the MAST reciprocating probe (RP) system,²³

TABLE II. Plasma parameters for MAST shots 28 819, 28 830, and 28 834. I_p is the plasma current, B_T is the toroidal field on axis, $n_{e,LCFS}$ is the plasma density at the last closed flux surface (LCFS) and \bar{n}_e is the line integrated plasma density.

Shot	$I_p(kA)$	$B_T(T)$	$n_{e,LCFS}(10^{19}m^{-3})$	$\bar{n}_e(10^{18}m^{-2})$
28 819	400	0.585	0.8	120
28 830	600	0.585	0.8	110
28 834	600	0.585	0.3	70

which has a slow motorized drive for initial placement of the probe and a fast pneumatic drive for reciprocations into the plasma. The maximum velocity attainable by the probe head is 1 m/s. In the CDN configuration, the RP is located at the outboard midplane and each reciprocation occurs over a distance of 8 cm in major radius. The motion of the plasma edge is accounted for using an EFIT²⁴ reconstruction and profiles will be presented in terms of $R - R_{LCFS}$, where R is the major radius and R_{LCFS} is the radial location of the last closed flux surface (LCFS). This is subject to a systematic error of ≤ 2 cm; however, this error is included in all results and is accounted for when making cross-diagnostic comparisons, so has no significant impact on conclusions in this paper.

To construct radial profiles of measured quantities, raw signals are split into 50 temporal bins with a width of 2.4 ms. On this time-scale, the RP is stationary allowing an average of the data to be taken within each bin. Each bin contains ≈ 1200 data points which reduces the error on the mean to an insignificant level. Any systematic offset errors have been accounted for by calibration against a control case, where no plasma is present.

III. BPP POTENTIAL MEASUREMENTS

Figure 3 shows the radial variation of the potential measured by the BPP (diamonds) and by the LP (squares) during reciprocation into the plasma in shots 28 819, 28 830, and 28 834. The error bars indicate the variance of the data within the bin, not the error on the mean. The random error on the mean is approximately 35 times smaller than the error bars shown. The first and most striking observation to be made from Figure 3 is that the BPP signal cannot simply be a suppressed version of the LP signal. In all three shots, the BPP shows regions of opposite polarity to the floating potential. This fits with the expectation from Eq. (1) that the floating potential should always be more negative than the BPP signal. Second, the radial profile of the BPP signal differs with respect to that of the floating potential. The BPP and V_{fl} profiles diverge as the probe penetrated the LCFS, in agreement with expression 1 where an increasing electron temperature should increase the deviation between V_{BPP} and V_{fl} .

The measured BPP signal demonstrates the qualitative features suggested by expression 1. To test the validity of the BPP measurement quantitatively, a comparison will be made with the electron temperature measurement from the Thomson scattering diagnostic.²²

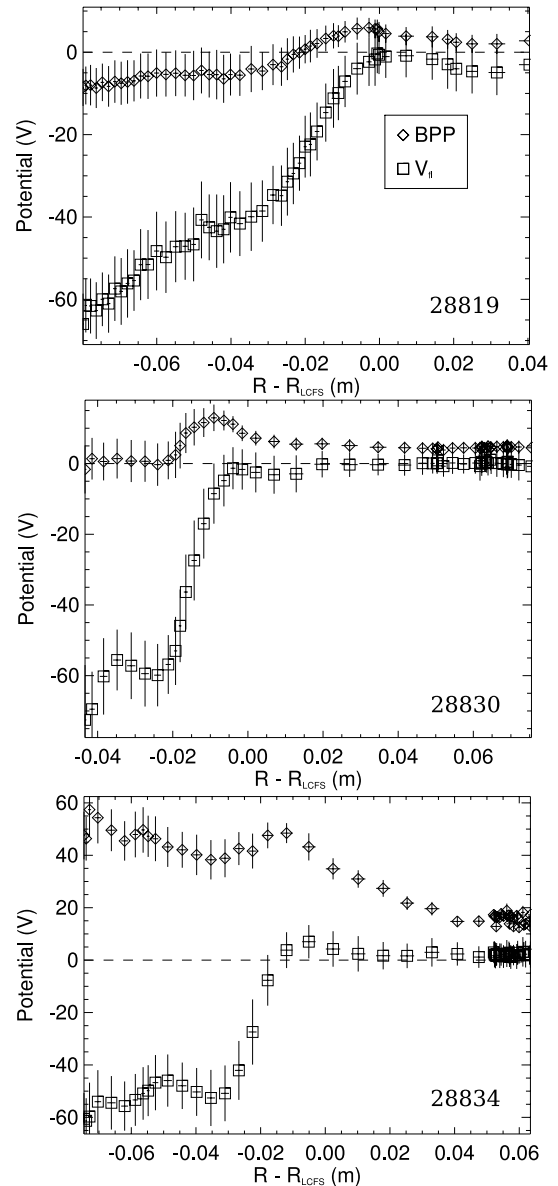


FIG. 3. Potential profiles measured by the BPP (diamonds) and the LP (squares). Error bars show the variance within each bin which is dominated by random fluctuations. The error on the mean is ≈ 35 times smaller than the error bars shown.

IV. ELECTRON TEMPERATURE MEASUREMENTS

Taking Eq. (1) and subtracting the floating potential from the BPP from the floating potential of a LP give an estimate of the electron temperature, T_e of

$$T_e \approx \frac{V_{BPP} - V_{fl}}{\alpha_{LP} - \alpha_{BPP}}. \quad (3)$$

The uncertainty on both α_{BPP} and α_{LP} leads to a range of values of the denominator in Eq. (3). Uncertainty in α_{LP} , given in Eq. (2), arises from uncertainty in T_i/T_e . Previous measurements on MAST have shown that $1 \leq T_i/T_e \leq 2.5$ is reasonable for L-mode conditions.²⁵⁻²⁷ This then gives $\alpha_{LP} = 2.7 \pm 0.1$. Since α_{BPP} cannot be measured directly in the system described in this paper, the empirical value of $\alpha_{BPP} = 0.6 \pm 0.3$ ^{6,10,12,14} found across a number of experiments is adopted. Recently, this approach has produced

electron temperature profiles on COMPASS and AUG in close agreement with Thomson scattering measurements.¹⁴ Taking these values of α_{LP} and α_{BPP} leads to a range of values for the denominator of Eq. (3) of

$$\alpha_{LP} - \alpha_{BPP} = 2.1 \pm 0.4, \quad (4)$$

which is used here to give a central, maximal, and minimal temperature measured from the BPP. MAST has a well resolved (spatially and temporally) TS diagnostic²² which is used as a comparison with the electron temperature derived from the BPP data. The TS data are sampled in a phase of the plasma shot, where the edge is approximately stationary. The data are binned in radius and averaged with error bars representing the standard error on the mean. Error on the TS data is a combination of random error associated with the measurement technique and the variance of fluctuations within the binning window. Data points with a random error greater than half the signal were rejected (in practice, this was not a significant portion of the data set). The comparison between the BPP and the TS diagnostic is shown in Figure 4.

The TS data lie within the range of uncertainty of the BPP data in each case. Whilst this is encouraging, the uncertainty on $\alpha_{LP} - \alpha_{BPP}$ is large and results primarily from uncertainty on α_{BPP} . Furthermore, the BPP measurement appears to be systematically lower than the TS measurement, with the disparity between the two measurements increasing at higher electron temperatures. By comparing the BPP measurement with the TS measurement, α_{BPP} can be constrained independently of the empirical value derived elsewhere. In order to accurately constrain α_{BPP} , however, α_{LP} must be specified as accurately as possible. In particular, the effects of secondary electron emission have, thus, far been neglected. This is a common practice in the case of flush-mounted probes where the magnetic field line incidence onto the probe is shallow and any emitted electrons are recaptured within a Larmor orbit. In the present case, however, the magnetic field has a near normal incidence on the probe surface and emitted electrons are accelerated away along the magnetic field line; as a result, secondary electron emission may be an important effect. Including the effects of secondary electron emission, α_{LP} is given by Ref. 19,

$$\alpha_{LP} = -\frac{1}{2} \ln \left(2\pi \frac{m_e}{m_i} \left(1 + \frac{T_i}{T_e} \right) (1 - \delta_e)^{-2} \right), \quad (5)$$

where δ_e is the ratio of secondary electrons emitted per primary incident electron. δ_e can be calculated for a graphite probe tip from the semi-empirical formula,^{19,28}

$$\delta_e = 2.72^2 \frac{E}{300} \exp \left(-2 \left(\frac{E}{300} \right)^{1/2} \right), \quad (6)$$

where E is the incident electron energy. From this expression, the secondary electron emission as a function of electron temperature, $\bar{\delta}(T_e)$ can be obtained by integration over a Maxwellian

$$\bar{\delta}(T_e) = \frac{\int_0^\infty \delta(E) \exp[-E/T_e] dE}{\int_0^\infty \exp[-E/T_e] dE}, \quad (7)$$

where E is in eV. Note that δ has been assumed here to be constant in pitch angle. Figure 5 shows $\delta(E)$ and $\bar{\delta}(T_e)$.

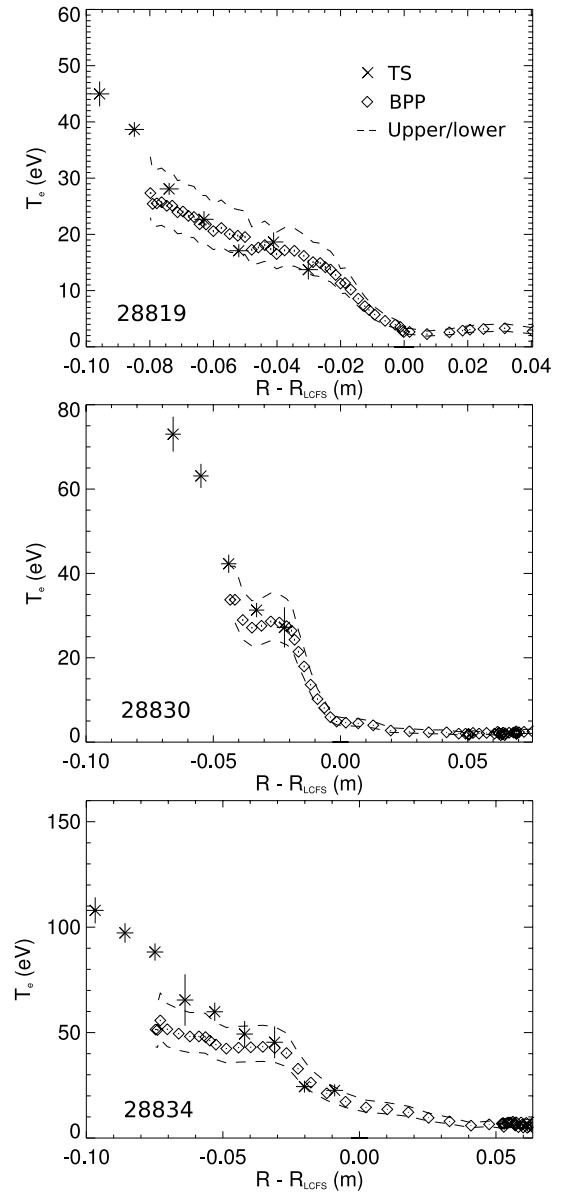


FIG. 4. Electron temperature measured by the BPP (diamonds) with upper and lower bounds (lines) compared to the TS measurement (stars). Upper and lower bounds are obtained by taking the extreme values from expression (4).

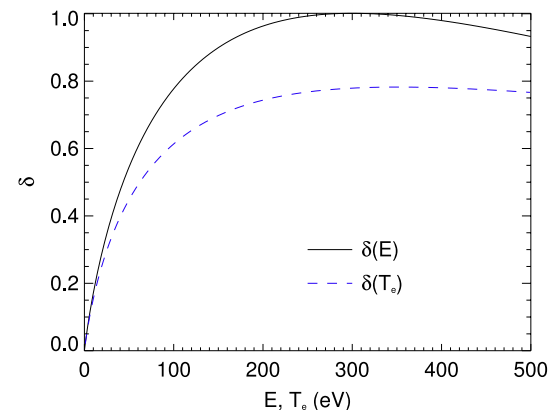


FIG. 5. Secondary electron yield as a function of energy, $\delta(E)$ calculated from expression 6, and as a function of electron temperature, $\bar{\delta}(T_e)$ calculated by integration over a Maxwellian.

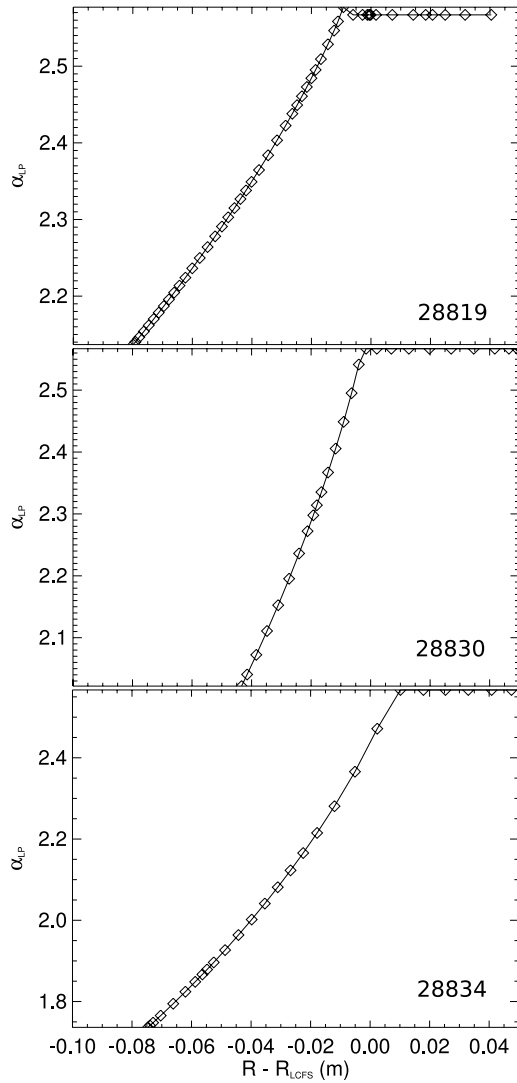


FIG. 6. Profiles of α_{LP} including the effects of secondary electron emission.

Experimentally, the secondary electron emission has been shown to increase as the angle of incidence reduces;²⁹ however, no parameterization of this effect exists. As such expression 6, which relates formally to normal incidence electrons, must be used. It should be noted though that this then gives an underestimate of the effect of secondary electron emission.

With the secondary electron yield parameterized as a function of T_e , α_{LP} can be calculated. This is achieved by taking a linear regression of the TS data, shown in Figure 4, to the point where $T_e < 1$ eV, beyond which the profile is set at $T_e = 1$ eV. This captures the main aspects of the temperature variation during the probe reciprocation and more detailed fits to the data were found to be unnecessary. This approximation to T_e is used as input to Eq. (5) and a radial profile of α_{LP} is produced. Figure 6 shows the profile of α_{LP} obtained with this technique in each shot. In these calculations, $T_i = 2T_e$ was assumed, which is motivated by previous measurements on MAST.^{25–27} Figure 6 shows that the secondary electron emission can have a major impact on the calculation of α_{LP} . It also causes α_{LP} to vary radially, which can affect the profile shape of the temperature measurement. It should be noted that a radial variation of α_{BPP} cannot be ruled out without a fuller

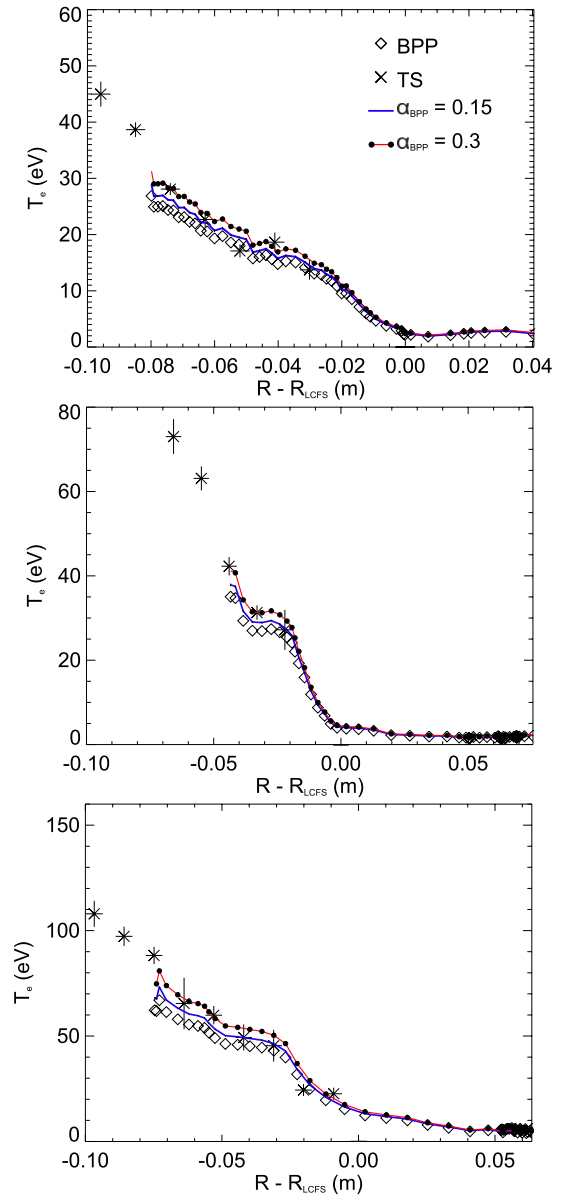


FIG. 7. BPP measurements of T_e , accounting for secondary electron emission, compared to TS data (crosses). The BPP data show the case of $\alpha_{BPP} = 0$ (diamonds), $\alpha_{BPP} = 0.15$ (solid blue line), and $\alpha_{BPP} = 0.3$ (dotted red line).

understanding of the BPP collection mechanism; however, direct measurements of α_{BPP} have yet to reveal such a radial variation.⁶ The values of α_{LP} can now be used to re-calculate the BPP measurement of T_e . This is shown in Figure 7.

By accounting for secondary electron emission, the BPP measurement of T_e agrees well with the TS data. The majority of the TS data, particularly in the hotter region inside the separatrix, lie between the BPP measurements obtained with $\alpha_{BPP} = 0$ (diamonds in Figure 7) and $\alpha_{BPP} = 0.3$ (red, dotted line in Figure 7). Outliers to this trend occur in the lowest temperature region, near to the separatrix and scrape off layer (SOL). In these regions, the TS data hit a floor measurement of 5 eV which can artificially raise the TS average. Furthermore, the random error on the TS data is much larger in these regions. The more reliable region of comparison occurs towards the hotter end of the profile. Assuming that the true value of α_{BPP} remains constant between all three shots, these results

suggest that α_{BPP} for the BPP on MAST can be constrained by $0 \leq \alpha_{BPP} \leq 0.3$. This is at the lower end of the values previously recorded in literature. This may be due to the lack of a conical collector, with the MAST collector being entirely flat. The conical shape allows for a portion of electron and ion currents to intersect the collector with a normal incidence along the field line. By removing the conical shape, the transport to the collector must occur perpendicularly to the magnetic field and is likely to be closer to ambipolar than the conical design. This may result in a reduced α_{BPP} in the case of a flat collector, as observed here. As indicated earlier, the lack of accounting for pitch angle in the calculation of the secondary electron emission suggests that these results are underestimates of the true BPP temperature. Accounting for pitch angle can provide an enhancement to the secondary electron emission by up to $\sim 40\%$.²⁹ Applying an artificial enhancement of this magnitude to the secondary electron emission was observed to bring the BPP and TS measurements into close agreement with $\alpha_{BPP} \approx 0$.

V. MEASUREMENTS OF THE RADIAL ELECTRIC FIELD

By cross-diagnostic comparison, the BPP has been shown to make a direct measurement of a quantity which can be (at least approximately) identified with the plasma potential. The plasma potential in itself is an interesting measurement; however, a more practically useful quantity is the radial electric field. The radial shear layer, a region of strong velocity shear near to the LCFS, is likely to play a key role in the anomalous transport of particles and energy into the SOL.³⁰ To leading order, the velocity in the shear layer results from $\mathbf{E} \times \mathbf{B}$ motion so is predominantly characterized by the radial electric field itself. This provides strong motivation for accurate measurements of the radial electric field.

The BPP signal can be corrected to measure the true plasma potential by the relation

$$\phi = V_{BPP} + \alpha_{BPP} T_e = (1 + \gamma) V_{BPP} - \gamma V_{f1}, \quad (8)$$

where $\gamma = \alpha_{BPP} / (\alpha_{LP} - \alpha_{BPP})$. Clearly, if $\alpha_{BPP} = 0$, the BPP measurement of the plasma potential is exact, however, given the uncertainty in the experimental comparison with the TS system, it is not possible to eliminate the possibility of finite α_{BPP} . As such it is important to assess how this uncertainty may affect measurements of the radial electric field. The BPP signal can be corrected by using the BPP calculation of T_e in Eq. (8). Figure 8 shows the corrected BPP measurement of the plasma potential, obtained by taking $\alpha_{BPP} = 0, 0.15$ and 0.3 , respectively. The effect of varying α_{BPP} on the plasma potential increases as the electron temperature grows and the corresponding correction to ϕ grows. The difference between the measured potential profiles can be significant, which is particularly true in shot 28 830. To see how this uncertainty affects the radial electric field measurements, the radial electric field is taken as the derivative of the BPP profiles in Figure 8 with respect to $\hat{R} = R - R_{LCFS}$ (to negate the effect of plasma edge motion) such that $E_R = -\nabla\phi = -\partial\phi/\partial\hat{R}$. To take the derivative, the BPP profile is fitted to a 17th degree polynomial (fits shown

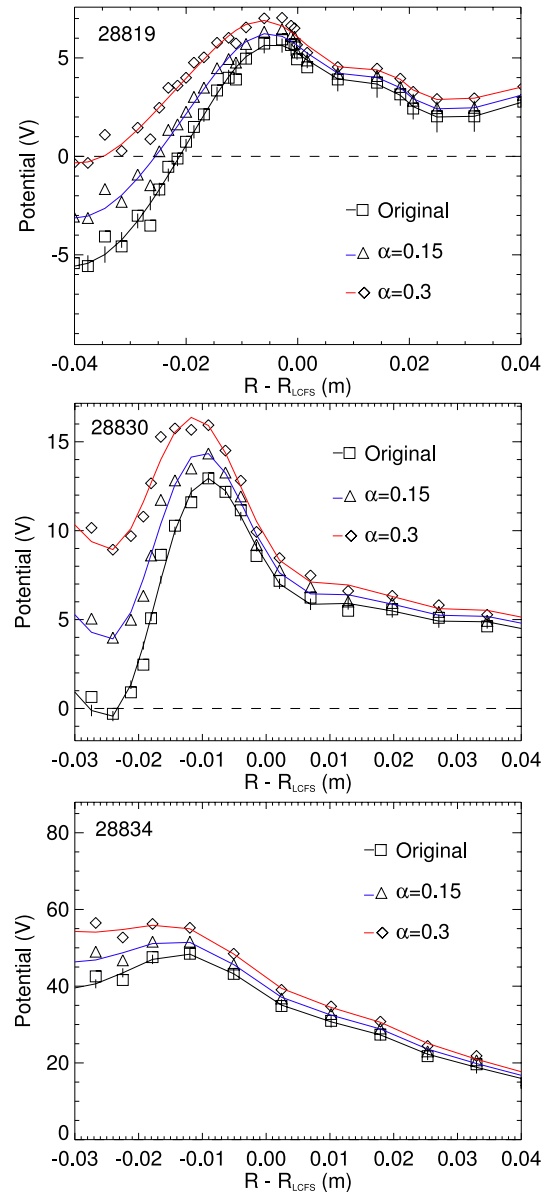


FIG. 8. Corrected BPP measurements of the plasma potential taking $\alpha_{BPP} = 0$ (black squares), $\alpha_{BPP} = 0.15$ (blue triangles), and $\alpha_{BPP} = 0.3$ (red diamonds). The uncertainty on the potential measurement grows as the probe moves deeper into the plasma, where the electron temperature increases and the consequential correction to the BPP potential grows. Solid lines show a 17th degree polynomial fit, used to obtain continuous profiles with a view to taking the derivative.

as solid lines in Figure 8) and the derivative is subsequently taken. Since no functional form of the radial electric field at the LCFS is present in the literature, a fitting function was chosen that provided a smooth profile, whilst capturing all of the important profile features. The radial electric field measurements, constructed in this manner, for shots 28 819, 28 830, and 28 834 are shown in Figure 9. The structure of the radial electric field measured on MAST agrees qualitatively with BPP and Doppler Reflectometry measurements on ASDEX-Upgrade.³¹ In each shot, a shear-layer can clearly be identified where the radial electric field changes sign. The magnitude of the electric field in the shear layer is on the order of ~ 1 kV/m which agrees with previous studies on MAST.^{32,33} The uncertainty induced by the variation in α_{BPP} in the measurement of E_R

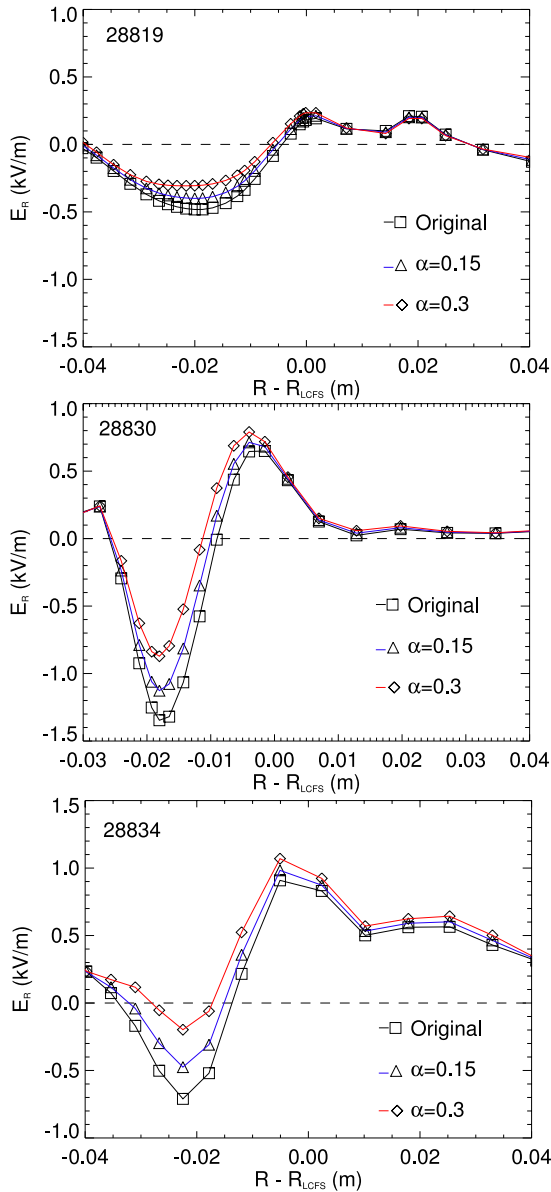


FIG. 9. Estimates of the radial electric field obtained by fitting a high order polynomial to the data presented in Figure 8 and taking $E_r \approx -\partial_r V_{BPP}$ for the correction factors $\alpha_{BPP} = 0$ (black squares), $\alpha_{BPP} = 0.15$ (blue triangles) and $\alpha_{BPP} = 0.3$ (red diamonds). The greatest uncertainty in the E_R occurs in the negative well on the inside of the radial shear layer.

is significantly less pronounced than in the plasma potential measurement. The uncertainty is most significant in the negative electric field well that occurs on the inside of the radial shear layer, where it can reach a level $\sim \pm 0.4$ kV/m; however, the uncertainty is reduced below this level over much of the profile. As a consequence, the BPP can be considered to make a well resolved estimate of E_R . Indeed, since the qualitative features of the radial electric field are independent of α_{BPP} , to a good approximation, the raw BPP data can be used to infer the radial electric field if α_{BPP} is unknown. The results in Figure 9 show a systematic increase in the magnitude of the radial electric field between shot 28 819 and shots 28 830 and 28 834. The principle difference between these two shots is the plasma current (see Table II) hinting that the radial electric field increases in magnitude (and consequently shear) with plasma

current. The relative similarity between the measurements in shots 28 830 and 28 834 in both magnitude and shear shows that increased density seems to play a lesser role in the formation of the radial electric field. The BPP offers the opportunity for further study of the scaling behaviour of the radial electric field and, of particular interest, the radial electric field shear and may therefore be a valuable tool in the effort to understand plasma transport in the tokamak periphery.

Using the radial profile of the toroidal and poloidal magnetic field taken from an EFIT reconstruction, a poloidal and toroidal $\mathbf{E} \times \mathbf{B}$ velocity estimate can be inferred, respectively. By separating the poloidal and toroidal components of $\mathbf{E} \times \mathbf{B}/B^2$, the velocity components can be given by

$$v_\theta = -\frac{B_\zeta E_R}{B^2} \approx -\frac{B_\zeta}{B^2} \frac{\partial V_{BPP}}{\partial R}, \quad (9)$$

$$v_\zeta = \frac{B_\theta E_R}{B^2} \approx -\frac{B_\theta}{B^2} \frac{\partial V_{BPP}}{\partial R}, \quad (10)$$

where B_θ is the poloidal magnetic field strength, B_ζ is the toroidal magnetic field strength, and B is the total magnetic field strength. The calculated v_θ and v_ζ are shown in Figure 10. The velocities are calculated using the E_R profiles with $\alpha_{BPP} = 0$ and represent velocity profile estimates containing the maximum possible shear from the BPP data. Radial profiles of B_ζ , B_θ , and B are used in these calculations; however, minimal variation is observed across the range of radii used. The plasma is observed to rotate poloidally and toroidal with a magnitude on the order of ~ 1 km/s. The comparative increase in the poloidal component over the toroidal component is a result of the weaker poloidal magnetic field. The shear in the radial electric field leads to a velocity shear layer which can be clearly identified in each shot once again about the point where the velocity changes sign. In the future, it is hoped that measurements such as these can be compared to other diagnostic systems on MAST, DBS (Doppler back-scattering), for example, to both increase the accuracy of velocity measurement on MAST and help to further constrain the uncertainty in the BPP measurements.

VI. DISCUSSION

This paper presents an iteration of the ball pen probe technique which has been developed to study the plasma potential on the spherical tokamak MAST. The ball pen probe illustrated in Figure 1 differs from the design of Adamek *et al.*⁶ in that the collector is flat, rather than conical. The design presented here closely resembles the design of Schrittwieser *et al.*⁹ which is based on the Katsumata probe (KP, also referred to as an ion-sensitive probe).³⁴ The use of a flat collector prevents current equalization by partial electron shielding, as proposed by Adamek *et al.*,⁶ from explaining the observed measurement of the plasma potential. Furthermore, since the collector is recessed deeper than the ion Larmor radius, both the ions and electrons are prevented from impacting the collector along the magnetic field line. The presence of a signal measured by the probe thus implies that cross field transport processes must be responsible. This is further evidenced by results in Refs. 6 and 7 where a

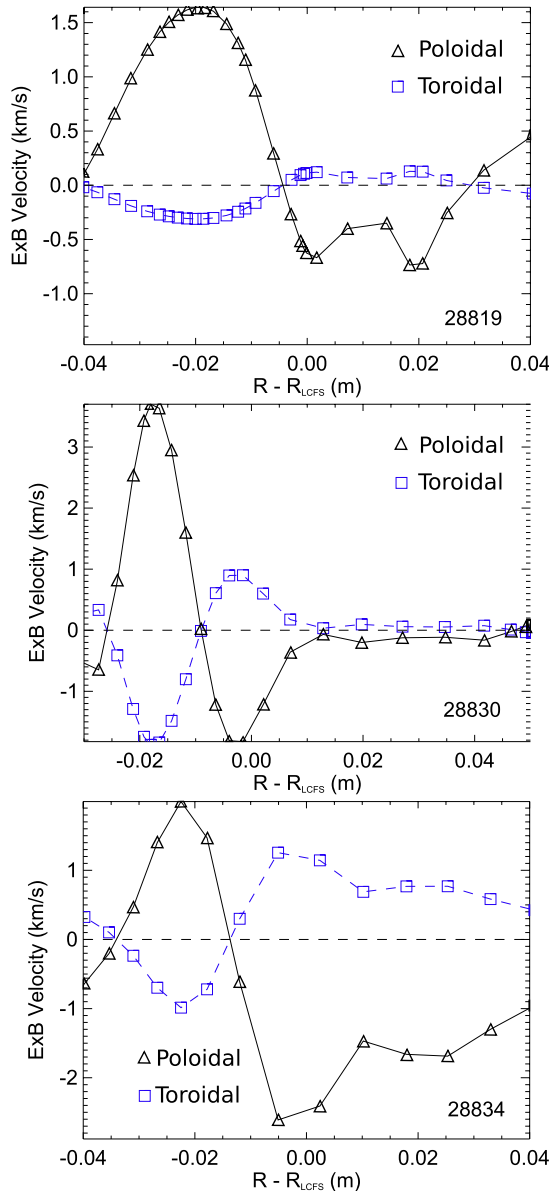


FIG. 10. Toroidal (blue squares) and poloidal (black triangles) velocities in the shear layer inferred from the E_r estimates in Figure 8 and using $v_{pol} \approx E_r/B_{tor}$ and $v_{tor} \approx E_r/B_{pol} \cdot B_{tor}$ and B_{pol} are taken from and EFIT reconstruction.

conventional design BPP is shown to measure the plasma potential even when the collector is retracted entirely within the shielding tube. Since cross-field transport is predominantly mediated by $\mathbf{E} \times \mathbf{B}$ motion which transports electrons and ions at the same rate, this can explain the observation of similar levels of electron and ion current at the collector, thereby causing the probe to float at the plasma potential. Sullivan *et al.*³⁵ have demonstrated experimentally that cross field $\mathbf{E} \times \mathbf{B}$ motion is responsible for transport of ions and electrons in a KP, with the perpendicular electric field generated by external biasing of the shielding walls. In a BPP, the situation is complicated by the fact that any electric fields within the shielding tube are setup by the plasma itself since the shielding walls are insulating. Predicting the structure of this electric field is far beyond the scope of this paper or indeed any current theory of the BPP; however, by considering the

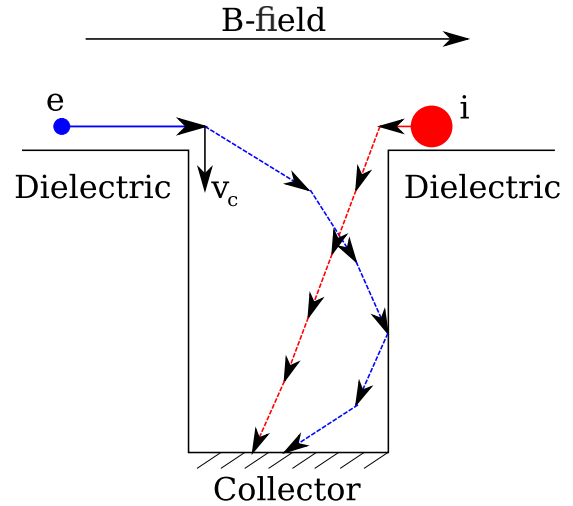


FIG. 11. Schematic illustration of the proposed mechanism for BPP collection in the case where the collection surface is flat and is retracted below the ion Larmor radius.

effect of the probe geometry on the collection of ions and electrons, some basic remarks can be made. Assuming that both ions and electrons are transported down the shielding tube at a typical velocity v_c , a condition can be placed on the parallel velocity of the ions of $v_{\parallel} > v_c d/h$, where d is the probe diameter and h is the probe retraction depth. This condition requires that ions travel down the tube faster than they can travel across the tube, otherwise they are lost to the shielding walls. Electrons, being many times more mobile than ions, are unlikely to adhere to this condition and may thus impact the shielding walls forming a sheath. As a result, electrons are repelled by the shielding walls whilst being transport down towards the collector. These processes are outlined schematically in Figure 11. The ion current to the collector can now be estimated as

$$I_i = An_i v_c \int_{v_c d/h}^{v_c d/h} \hat{f}_i dv_{\parallel}$$

and the electron current by

$$I_e = An_e v_c \int_{v_{sh}}^{v_{sh}} \hat{f}_e dv_{\parallel} \approx An_e v_c,$$

where $\hat{f}_{i,e}$ is the normalized one-dimensional Maxwellian $f_m(v_{\parallel}) / \int_{-\infty}^{\infty} f_m(v_{\parallel}) dv_{\parallel}$. v_{sh} is the electron parallel velocity required to overcome sheath repulsion, $n_i = n_e$ is the ion/electron density, and A is the collection area of the probe. Using these expressions, α_{BPP} can be approximated as

$$\alpha_{BPP} = \ln(I_e/I_i) = -\ln\left(\int_{v_c d/h}^{v_c d/h} \hat{f}_i dv_{\parallel}\right). \quad (11)$$

Thus to achieve, for example, $\alpha_{BPP} = 0.6$, a probe with the geometry of BPP2 (described in Table I) in a plasma with an ion temperature of 10 eV will require a collection velocity of $\sim 10 - 50$ km/s which is comparable to the acoustic speed. Furthermore, this suggests that for a given collection velocity, α_{BPP} may be reduced by maximizing the ratio d/h (keeping h below the ion Larmor radius). Taking a simple estimate for the internal electric field provided by sheath formation on the shielding walls as $E \sim 2T_e/d$, the resulting $\mathbf{E} \times \mathbf{B}$ velocity is

~ 10 km/s, which is on the correct scale to give the empirical values of α_{BPP} obtained here and elsewhere. The arguments laid out here also suggest that α_{BPP} may be temperature dependent, a factor which has not been considered in the experimental comparison conducted in this paper but would be a good topic for future study.

Naturally, there are many other factors that complicate this proposed collection mechanism; collisions, ion space charge within the shielding tube, ion orbit variation and turbulent transport in the vicinity of the probe to name a few. Clearly, a system of this complexity does not lend itself to analytical considerations and to properly capture BPP collection; it is likely that reliable 3D3V particle-in-cell simulations will be required. These should be accompanied by dedicated experimental testing of the diagnostic with differing geometries to isolate what factors affect BPP collection. At present, neither of these approaches is available and so it is necessary to resort to cross-diagnostic comparison for validation purposes, as conducting in this paper.

VII. CONCLUSIONS

The ball pen probe technique has been successfully used on MAST to make profile measurements of potential, electron temperature, and radial electric field. It has been shown to make a measurement which lies much closer to the true plasma potential than the floating potential and is demonstrated to behave differently to the floating potential both in terms of polarity and profile shape. By combining the BPP measurement with the standard measurement of floating potential from a Langmuir probe, the electron temperature profile has been derived and compared favourably to a complementary measurement made by the MAST Thomson scattering system. This constrains the parameter α_{BPP} to $0 \leq \alpha_{BPP} \leq 0.3$. In making the diagnostic comparison between the BPP and the TS system, accounting for secondary electron emission was shown to be important in constraining α_{BPP} . More generally, this suggests that the effect of secondary electron emission should be accounted for when interpreting probe data where the field line incidence to the probe is close to normal. By fitting a polynomial function to the BPP potential profiles and taking the derivative with respect to distance from the LCFS, the radial electric field is measured for Ohmic L-mode MAST plasmas. It is shown to exist on the order of ~ 1 kV/m and appears to increase with increasing plasma current. Uncertainty in the measurement is relatively low but reaches its highest point in the negative well of the electric field, inside the radial shear layer. From these estimates, a toroidal and poloidal rotation velocity can be inferred by taking appropriate values of the poloidal and toroidal magnetic field, respectively.

This paper highlights the capability of the ball pen probe to make several useful and important measurements in the plasma edge. Furthermore, it has a robust design capable of operation well inside the LCFS. The specific design used for MAST was a straightforward modification of an existing probe-head showing the ease with which a ball pen probe can be implemented. A drawback of the technique is an imprecise understanding of its collection mechanism; however, it is

hoped that the empirical success of the ball pen probe motivates continued use of this technique in the study of boundary plasma phenomena.

ACKNOWLEDGMENTS

This work has been carried out within the framework of the EUROfusion Consortium and has received funding from the Euratom research and training programme 2014-2018 under grant agreement No 633053, from the RCUK Energy Programme [grant number EP/I501045], by project GA CR P205/12/2327 of the Grant Agency of Czech Republic, by project MSMT LM2011021, by the Czech Science Foundation GA14-12456S and by the European Communities. To obtain further information on the data and models underlying in this paper, please contact Publication-Manager@cce.ac.uk. The views and opinions expressed, herein, do not necessarily reflect those of the European Commission. Finally, we would like to thank the MAST Team.

- ¹S. I. Braginskii, *Reviews of Modern Physics* (Consultants Bureau, New York, 1965), Vol. 1, p. 205.
- ²A. N. Simakov and P. J. Catto, *Phys. Plasmas* **20**, 4744 (2003).
- ³A. N. Simakov and P. J. Catto, *Phys. Plasmas* **11**, 2326 (2004).
- ⁴F. Militello *et al.*, *Plasma Phys. Controlled Fusion* **55**, 025005 (2013).
- ⁵N. R. Walkden, B. D. Dudson, and G. Fishpool, *Plasma Phys. Controlled Fusion* **55**, 105005 (2013).
- ⁶J. Adamek *et al.*, *Czech. J. Phys.* **54**, C95 (2004).
- ⁷J. Adamek *et al.*, *Czech. J. Phys.* **55**, 235 (2005).
- ⁸J. Adamek *et al.*, *Contrib. Plasma Phys.* **54**, 279 (2014).
- ⁹R. J. Schrittwieser *et al.*, *Czech. J. Phys.* **56**, B145 (2006).
- ¹⁰J. Adamek *et al.*, *J. Nucl. Mater.* **390-391**, 1114 (2009).
- ¹¹J. Adamek *et al.*, *Contrib. Plasma Phys.* **50**, 9 (2010).
- ¹²J. Horacek *et al.*, *Nucl. Fusion* **50**, 105001 (2010).
- ¹³C. Silva, J. Adamek, H. Fernandes, and P. Duarte, in *40th EPS conference on plasma physics, Espoo, Finland* (Conference proceedings, 2013), P5.103.
- ¹⁴J. Adamek *et al.*, in *41st EPS Conference on Plasma Physics, Berlin, Germany, 2014*.
- ¹⁵J. Adamek *et al.*, *Contrib. Plasma Phys.* **53**, 1 (2013).
- ¹⁶M. Cox and MAST Team, *Fusion Eng. Des.* **46**, 397 (1999).
- ¹⁷P. Taaian *et al.*, *Plasma Phys. Controlled Fusion* **52**, 075017 (2010).
- ¹⁸I. H. Hutchinson, *Principles of Plasma Diagnostics*, 2nd ed. (Cambridge University Press, 2001).
- ¹⁹P. C. Stangeby, *The Plasma Boundary of Magnetic Fusion Devices* (Taylor and Francis, New York, 2000).
- ²⁰M. Komm, J. Adamek, Z. Pekarek, and R. Panek, *Contrib. Plasma Phys.* **50**, 9 (2010).
- ²¹M. Komm *et al.*, *Plasma Phys. Controlled Fusion* **53**, 015005 (2011).
- ²²R. Scannell *et al.*, *Rev. Sci. Instrum.* **77**, 10E510 (2006).
- ²³Y. Yang, G. Counsell, and MAST Team, *J. Nucl. Mater.* **313-316**, 734 (2003).
- ²⁴L. L. Lao *et al.*, *Nucl. Fusion* **25**, 1611 (1985).
- ²⁵S. Elmore *et al.*, *Plasma Phys. Controlled Fusion* **54**, 065001 (2012).
- ²⁶S. Elmore, S. Y. Allen, A. Kirk, and A. J. Thornton, *J. Nucl. Mater.* **438**, S1212 (2013).
- ²⁷S. Y. Allan *et al.*, *J. Nucl. Mater.* **438**, S1192 (2013).
- ²⁸E. W. Thomas, Atomic and plasma-material interaction data for fusion, Suppl. to *Nuclear Fusion* **1**, 79 (1991).
- ²⁹M. E. Woods *et al.*, *J. Phys. D: Appl. Phys.* **20**, 1136 (1987).
- ³⁰G. S. Xu *et al.*, *Nucl. Fusion* **49**, 092002 (2009).
- ³¹H. W. Muller *et al.*, *Nucl. Fusion* **51**, 073023 (2011).
- ³²H. Meyer *et al.*, *J. Phys.: Conf. Series* **123**, 012005 (2008).
- ³³D. Temple, "Experimental investigations into the radial electric field of MAST," Ph.D. thesis (Imperial College London, 2011).
- ³⁴I. Katsumata, *Contrib. Plasma Phys.* **36**, S73 (1996).
- ³⁵R. M. Sullivan, R. Ochoukov, and D. G. Whyte, *J. Nucl. Mater.* **438**, S1253 (2013).